



Accounting for the effect of aerosols in GHGSat methane retrieval

Qiurun Yu¹, Dylan Jervis², and Yi Huang¹

¹Department of Atmospheric and Oceanic Sciences, McGill University, Montréal, QC H3A 0B9, Canada

²GHGSat, Inc., Montréal, QC H2W 1Y5, Canada

Correspondence: Qiurun Yu (qiurun.yu@mail.mcgill.ca)

Received: 8 December 2023 – Discussion started: 23 January 2024

Revised: 12 April 2024 – Accepted: 15 April 2024 – Published: 3 June 2024

Abstract. GHGSat comprises a constellation of satellites with high spatial and spectral resolution that specialize in monitoring methane emissions at 1.65 μm . This study investigates the ability to accurately retrieve both the methane mixing-ratio enhancement (ΔX_{CH_4}) and the aerosol optical depth (AOD) simultaneously from simulated GHGSat observations that incorporate angle-dependent scattering information. Results indicate that the sign of the ΔX_{CH_4} bias when neglecting aerosols changes from negative to positive as surface albedo increases, which is consistent with previous studies. The bias in ΔX_{CH_4} is most pronounced when AOD is not simultaneously retrieved, ranging from -3.0% to 6.3% with an AOD of 0.1, a 60° solar zenith angle, and a surface albedo of 0.2 for the nadir-only retrieval. Using multiple satellite viewing angles during the GHGSat observation sequence with a scattering angle ranging from 100 to 140° , the study shows that the mean bias and standard deviation of ΔX_{CH_4} are within 0.3% and 2.8% relative to the background. The correlation between simultaneously retrieved ΔX_{CH_4} and AOD shifts from being positive to negative as surface albedo increases and the aerosol asymmetry factor decreases, signifying a transition of the dominant aerosol effect from aerosol-only scattering to aerosol–surface multiple scattering. The variety of scattering angle ranges has little impact on the performance of the multi-angle viewing method. This study improves the understanding of the impact of aerosols on the GHGSat ΔX_{CH_4} retrieval and provides guidance for improving future GHGSat-like point-source imagers.

1 Introduction

Aerosols can modify photon path lengths via their scattering and absorption effects and have been identified as one of the major sources of errors when retrieving greenhouse gases from spectrally resolved backscattered solar radiation in the shortwave infrared (SWIR) (Aben et al., 2007; Butz et al., 2009; Connor et al., 2016; Chen et al., 2017; Huang et al., 2021). Accurately assessing greenhouse gas emissions in the presence of aerosols remains a challenge. This is because unaccounted-for aerosols can either enhance or reduce the absorption of light by gases, depending on factors such as the aerosol concentration, aerosol height distribution, viewing geometry, and surface albedo, among others (Butz et al., 2009; Frankenberg et al., 2012; Sanghavi et al., 2020). Houweling et al. (2005) analyzed Scanning Imaging Absorption Spectrometer for Atmospheric Cartography (SCIAMACHY) measurements of total-column CO_2 over the Sahara and found that the unrealistically large CO_2 variability of the total column, 10% (37 ppm), was caused by mineral dust aerosols. Butz et al. (2009) found that if aerosols are not considered, atmospheric CO_2 retrieval errors larger than 1% may occur when using SCIAMACHY and Greenhouse gases Observing SATellite (GOSAT)-like observers. These errors are dependent on both the surface albedo and the type of aerosols present. Huang et al. (2020) simulated Airborne Visible/Infrared Imaging Spectrometer – Next Generation (AVIRIS-NG) measurements for methane emissions. Their results show an underestimation of CH_4 resulting from aerosols, particularly those with a high single-scattering albedo and a low asymmetry factor (such as water-soluble aerosols). These studies, among many others, underlined the importance of understanding the effect of aerosols on the remote sensing of greenhouse gases.

To account for the atmospheric scattering in the SWIR satellite retrieval of greenhouse gas, a “full-physics” retrieval requires simultaneously solving for the vertical profile of gas concentration, aerosol extinction, and the surface reflectivity through the inversion of the radiance spectrum using a radiative-transfer model (Butz et al., 2012; Jacob et al., 2022). However, this method is time-consuming and is likely to fail if the atmosphere is heavily polluted or if the surface is too dark (Lorente et al., 2021). In contrast to “physics-based” methods, some proxy methods, which are much faster than full-physics retrieval and achieve similar precision and accuracy, have been proposed. To simultaneously retrieve the CO₂ total-column and aerosol properties, the “three-band” retrieval exploits measurements of the absorption bands of O₂ (0.77 μm) and CO₂ (1.61 and 2.06 μm) to retrieve the aerosol amount, height distribution, and size distribution based on a simple aerosol microphysical model (Butz et al., 2009). However, this approach requires additional consideration of the uncertainty of a prior estimate of CO₂ (Butz et al., 2012). According to Parker et al. (2020), the methane mixing ratio (X_{CH_4}) can be retrieved using both CH₄ (1.65 μm) and the adjacent CO₂ band (1.61 μm) by taking advantage of the $X_{\text{CH}_4}/X_{\text{CO}_2}$ ratio without accounting for atmospheric scattering. However, this “CO₂ proxy” method is subject to bias for sources that co-emit CH₄ and CO₂, such as gas flaring. Depending on the instrument design and its limitations, the approach to accounting for the effect of aerosols on greenhouse gas retrieval varies.

GHGSat, Inc., has developed a nano-satellite system that measures greenhouse gas emissions from individual industrial facilities (Varon et al., 2019). Its satellite achieves a combination of fine spatial resolution and spectral resolution by pointing at targeted methane point sources (Jervis et al., 2021; Jacob et al., 2022). As of the time of writing, GHGSat has launched a constellation of 11 commercial satellites (GHGSat-C1 to GHGSat-C11) which monitor methane emissions from natural-gas industry operations, landfills, hydroelectric reservoirs, and oil sand operations, among others (Calvello et al., 2017; Varon et al., 2019; Jacob et al., 2022; Maasackers et al., 2022). However, industrial activities such as oil extraction and pre-treatment involve not only gaseous emission but also aerosol production (e.g., water-soluble and black-carbon aerosols). The continued development of the GHGSat satellite requires identifying and minimizing the uncertainty in methane retrieval due to aerosol interference. Newer GHGSat satellites only target the CH₄ band; consequently, the above-mentioned “proxy” methods to account for the aerosol effects do not apply to their instrument. An accurate aerosol retrieval model for GHGSat would not only reduce the uncertainty in their methane retrieval but also provide a new aerosol data product, potentially allowing high-spatial-resolution air quality measurements from space.

The angular dependence of aerosol scattering allows space-borne observations of aerosol properties based on multi-angle measurements, which have the potential to miti-

gate aerosol-induced errors in current greenhouse gas satellite observations. Frankenberg et al. (2012) demonstrated that adding multiple satellite viewing angles to Orbiting Carbon Observatory 2 (OCO-2)-like observations enhances the ability to retrieve aerosol properties. The aerosol information can, in turn, significantly decrease errors in the measurement of CO₂ and CH₄ total columns. However, this multi-angle viewing method was applied to area flux mappers which are designed to observe emissions on regional scales. There has been little study of how to retrieve aerosols using point-source imagers like GHGSat. A method to co-retrieve aerosols and methane using GHGSat spectral content could address a gap in current research on point-source imagers, improve the accuracy of their greenhouse gas retrieval, and provide greater details about local aerosol and methane concentrations.

This study has three objectives. First, we assess how aerosols impact the accuracy of GHGSat methane mixing-ratio enhancement (ΔX_{CH_4}) retrieval when the aerosols are present but not retrieved. This assessment involves simulating GHGSat satellite observations for a wide range of aerosol optical properties and surface albedo values to evaluate the distribution and magnitude of any resulting bias in ΔX_{CH_4} under different aerosol and surface conditions. Second, we simultaneously retrieve the aerosol optical depth (AOD) and ΔX_{CH_4} using a multi-angle viewing method and perform a comparison with the ΔX_{CH_4} -only retrieval obtained under the same conditions. Finally, we investigate how different scattering angles as well as uncertainties in aerosol type, height distributions, and surface albedo affect the performance of the simultaneous retrieval.

This paper is organized into five sections. Section 2 provides an overview of the atmospheric models, the GHGSat instrument model, and the simultaneous retrieval methods for aerosols and methane. Section 3 evaluates the errors that occur in GHGSat methane retrieval under various aerosol, surface, and satellite zenith angle conditions. Synthetic data are used to conduct retrieval under two scenarios: methane-only nadir retrieval and the simultaneous retrieval of methane and aerosols using the multi-angle viewing method. Section 4 investigates the impact of satellite viewing angles as well as the uncertainty in aerosol and surface albedos on simultaneous retrieval. A summary is presented in Sect. 5.

2 Method

2.1 Atmospheric model

The top-of-the-atmosphere (TOA) radiance detected by the satellite comes from both direct and diffuse reflections. The incoming sunlight is reflected into space by the Earth’s surface and atmospheric scatterers such as aerosols. When the solar beam travels through the atmosphere, it can be partly absorbed along its path by atmospheric absorbers, such as

methane molecules and aerosols. Additionally, multiple scattering processes occur between the surface and aerosol layers. To assess the radiative impact of aerosols in the GHGSat methane retrieval, a forward model to simulate GHGSat-measured solar radiation is required.

The radiative-transfer forward model used in this study is DIScret Ordinate Radiative Transfer (DISORT) version 4.0.99 (Stamnes et al., 1988). As one of the most general and versatile plane-parallel radiative-transfer models, DISORT has been widely used for the remote sensing of greenhouse gases, aerosols, and clouds (Tzanis and Varotsos, 2008; Wang et al., 2013; Boiyo et al., 2019). It can numerically compute satellite-measured radiance at different wavenumbers using discrete vertical coordinates. For each atmospheric layer, the spectral optical depth and single-scattering albedo for atmospheric molecules are computed by using a rigorous line-by-line radiative-transfer model (LBLRTM) over a 0.1 cm^2 interval (Clough et al., 2005). The mid-latitude summer profile is chosen as the default atmospheric state. The absorption of four main atmospheric absorptive gases (H_2O , CO_2 , O_3 , and CH_4) at 45 layers is considered through line-by-line calculations.

To facilitate the analysis of aerosol-induced errors during the GHGSat CH_4 retrieval, this study focuses on the short-wave near-infrared band (1662–1672 nm). This band covers absorption lines which are mainly caused by CH_4 . The surface is assumed to be Lambertian, and we adopt the 16-stream approximation. With the specified viewing geometry and surface albedo, DISORT can calculate the solar radiation that is backscattered into space by the Earth's surface and atmosphere. For a clean atmosphere with a surface albedo of 0.2, the TOA upward radiance simulated by DISORT is shown in Fig. 1b. The solar zenith angle is 60° , and the satellite field of view is in the nadir position. In Fig. 1b, strong CH_4 absorptions are observed around 1666 nm, consistent with results from other studies like Jervis et al. (2021) and Chan Miller et al. (2023). Given that GHGSat measures methane concentrations by analyzing spectrally decomposed solar backscattered radiation within the methane absorption band ($\sim 1.65 \mu\text{m}$), this alignment supports the adequacy of DISORT-simulated radiance for capturing the methane effect. With the TOA incoming solar radiance known (Fig. 1a), the TOA reflectance ($\text{Ref}_\lambda^{\text{TOA}}$) can be calculated via

$$\text{Ref}_\lambda^{\text{TOA}} = \frac{\text{radiance}_\lambda^{\text{TOA}\uparrow}}{\text{radiance}_\lambda^{\text{TOA}\downarrow}}, \quad (1)$$

where $\text{radiance}_\lambda^{\text{TOA}\downarrow}$ and $\text{radiance}_\lambda^{\text{TOA}\uparrow}$ are the TOA downward and upward radiances at wavelength λ . The radiance is in units of $\text{W m}^{-2} \text{sr}^{-1} \text{m}^{-1}$. For GHGSat retrieval considering only gas absorbers, the relative depth of the absorption line directly corresponds to the retrieved methane enhancement compared to the background. Therefore, $\text{Ref}_\lambda^{\text{TOA}}$ is directly linked to the retrieved CH_4 enhancement and is shown in Fig. 1c.

2.2 Aerosol settings

Many factors, such as aerosol type, concentration, and height distribution, can impact the radiance measurement. In this study, the aerosol types are predefined in the retrieval. We used climatological aerosol optical-property values from Ayash et al. (2008) to account for the diverse range of particles found in industrial sites. For aerosols composed of multiple components, the single-scattering albedo (SSA) spans from 0.86 to 0.98, while the asymmetry factor (g) ranges from 0.54 to 0.76. GHGSat mainly focuses on measuring the CH_4 enhancement over methane hotspots, where CH_4 and the co-emitted aerosols are concentrated near the surface. To emulate the aerosol emissions from the industrial plume, one arbitrary aerosol layer is added near the surface between 1000 to 900 hPa. Considering the limitation of the instrument to one spectral band, the simplified treatment of aerosols in the forward model allows for a more direct physical interpretation of the effect of aerosols on methane retrieval. We focus mainly on the AOD retrieval because this variable is highly representative of the aerosol radiation effect (Frankenberg et al., 2012; Yu and Huang, 2023a, b). In this study, the simulated truth of the AOD is 0.1 at the SWIR (~ 0.3 AOD at 550 nm). This threshold is selected in the retrieval because it is used to filter values in other X_{CH_4} retrieval studies (Lorente et al., 2021).

2.3 The multi-angle viewing method

The multi-angle aerosol retrieval method proposed by Frankenberg et al. (2012) uses the radiance difference at various viewing geometries to retrieve aerosol information and takes advantage of the fact that aerosols scatter more light forward than backward. In this study, the satellite azimuth angles are chosen to be 0 and 180° to represent forward-viewing and backward-viewing observations (i.e., straight south- and north-looking), respectively. Table 1 summarizes the angles used in the multi-angle viewing simulations. The scattering angle Θ is calculated following Thompson et al. (2022) as

$$\Theta = 180^\circ - \arccos[\cos\theta_1 \cos\theta_2 + \sin\theta_1 \sin\theta_2 \cos(\varphi_1 - \varphi_2)], \quad (2)$$

where θ_1 and θ_2 are the solar and satellite zenith angles, respectively, and φ_1 and φ_2 are the solar and satellite azimuth angles, respectively. Figure 2 shows the schematics of the multi-angle viewing method and its corresponding angles. This study assumes the Henyey–Greenstein phase function for aerosols (Toublanc, 1996), which defines the phase function via

$$P_{\text{HG}}(\cos\Theta) = \frac{1 - g^2}{(1 - 2g \cos\Theta + g^2)^{3/2}}, \quad (3)$$

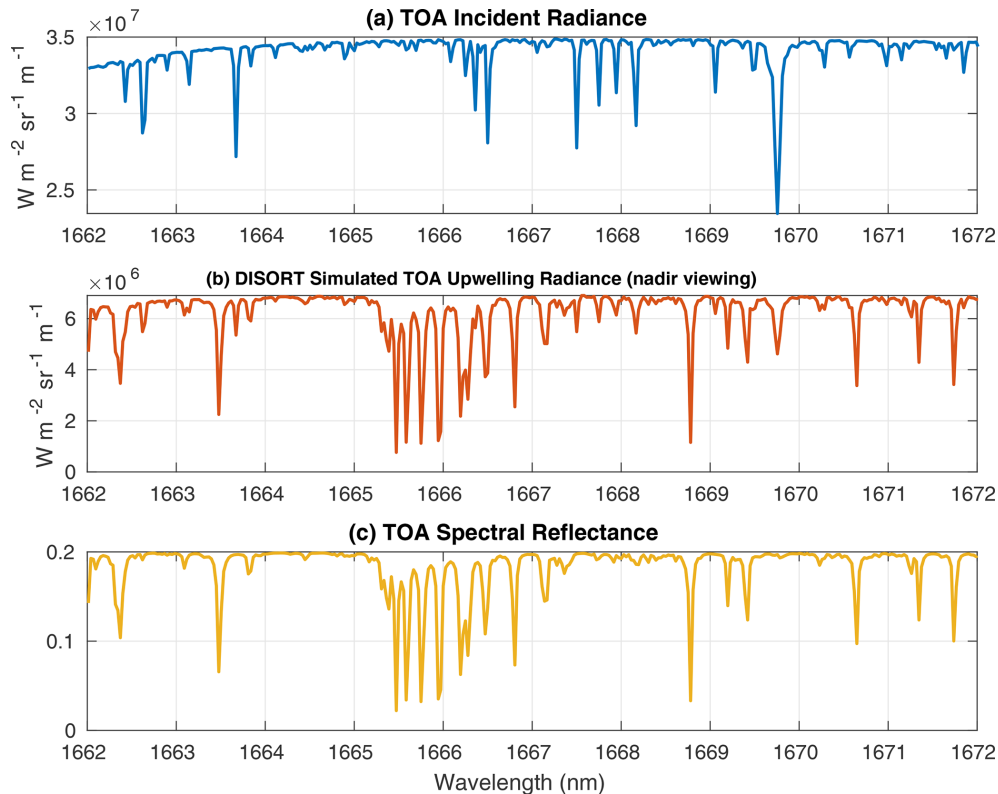


Figure 1. (a) TOA incoming solar radiance, (b) simulated TOA upward radiance (nadir viewing), and (c) spectral reflectance (nadir viewing). Spectra are simulated with a surface albedo of 0.2 and a solar zenith angle of 60° .

where g is the aerosol asymmetry factor. The high g value implies that most of the scattered light is directed forward in the same general direction as the incident light.

2.4 GHGSat instrument model

A nominal GHGSat measurement covers a targeted $12 \times 15 \text{ km}^2$ area with approximately $25 \times 25 \text{ m}^2$ pixel resolution and 0.3 nm spectral resolution (Jervis et al., 2021; Jacob et al., 2022). The instrument adjusts its altitude to ensure that the targeted area remains within its field of view for an extended period, thereby enhancing its signal-to-noise ratio (SNR). During the observation sequences, the GHGSat spectrometer typically takes 200 images of closely overlapping atmospheric absorption spectra. A more detailed description of the design of the GHGSat instrument and its measurement concept is presented in Jervis et al. (2021). To simulate GHGSat measurements, this study focuses on the spectral region between 1662 and 1672 nm and applies a Gaussian broadening kernel of 0.3 nm full width at half maximum (FWHM). Using the multi-angle viewing method, the satellite observes the target position from different angles, transitioning from a forward view to a view looking directly downward (nadir) and finally to a backward view.

As an example, Fig. 3 displays the simulated GHGSat radiance corresponding to the solar geometry detailed in Ta-

ble 1, under the assumption of a single layer of sulfate aerosols near the surface with an SSA of 1 and a g of 0.78. These simulations are based on a surface albedo of 0.2 and an AOD of 0.1 at the SWIR for illustration purposes. Figure 3 indicates that with the addition of a highly reflective aerosol layer, TOA reflectance in the forward viewing direction exceeds that in the nadir or backward viewing direction. This suggests the importance of viewing angles in GHGSat observations when aerosols are present and highlights the potential for retrieving them using multi-angle information. In the following discussions, a positive satellite zenith angle corresponds to an azimuth angle of 0° (forward viewing), while a negative zenith angle corresponds to an azimuth angle of 180° (backward viewing).

2.5 Retrieval methods

Figure 4 illustrates the steps in the simulated retrieval process in this study. First, we combine the atmospheric-molecule optical properties calculated from the LBLRTM with the aerosol optical properties to run the atmospheric model (DISORT). Then DISORT is further modified according to the GHGSat instrument design to build a complete forward model $F(\mathbf{X})$ to simulate the TOA reflectance (Eq. 1). \mathbf{X} is the state vector, which includes elements such as the methane mixing ratio X_{CH_4} , the aerosol optical depth (AOD), and the

Table 1. Angles used in the multi-angle satellite viewing simulations in Sects. 3.1 and 3.2.

	Solar zenith angle θ_1	Satellite zenith angle θ_2	Solar azimuth angle φ_1	Satellite azimuth angle φ_2	Scattering angle Θ
Forward viewing	60°	20°	180°	0°	100°
Nadir	60°	0°	180°	0°	120°
Backward viewing	60°	20°	180°	180°	140°

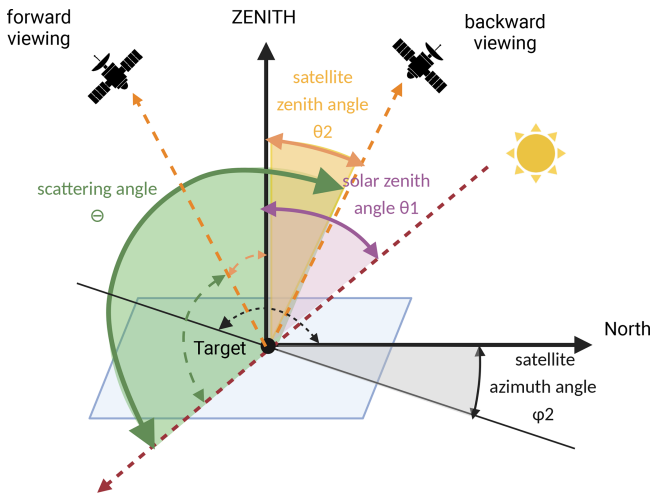


Figure 2. Schematic of a given solar and viewing geometry as well as the corresponding scattering angle for the forward and backward viewing modes. The solar zenith angle θ_1 , satellite zenith angle θ_2 , and satellite azimuth angle φ_2 are indicated by curved double arrows that are purple, orange, and black, respectively. The scattering angle Θ is represented by the curved green double arrow. The viewing angles for the backward and forward viewing modes are depicted using solid and dashed curved double arrows, respectively. In this case, the satellite azimuth angles are 0 and 180° for the backward and forward viewing directions (angles are relative to the north-facing vector).

surface albedo X_{alb} . The goal of the retrieval is to estimate ΔX_{CH_4} and X_{alb} for the ΔX_{CH_4} -only retrieval as well as to estimate ΔX_{CH_4} , AOD, and X_{alb} for the simultaneous retrieval using the multi-angle viewing method from the measurement vector y :

$$y = F(X) + \epsilon_y, \tag{4}$$

where ϵ_y is the measurement error.

Full GHGSat retrieval consists of two steps: a scene-wide retrieval to estimate the background average state vector \hat{X} and a per-cell retrieval to estimate the local methane plume enhancement. Note that the surface albedo is retrieved in both cases. In this study, we focus on the per-cell retrieval assuming a known background \hat{X} . In Jervis et al. (2021), a linearized forward model (LFM) is proposed for the GHGSat

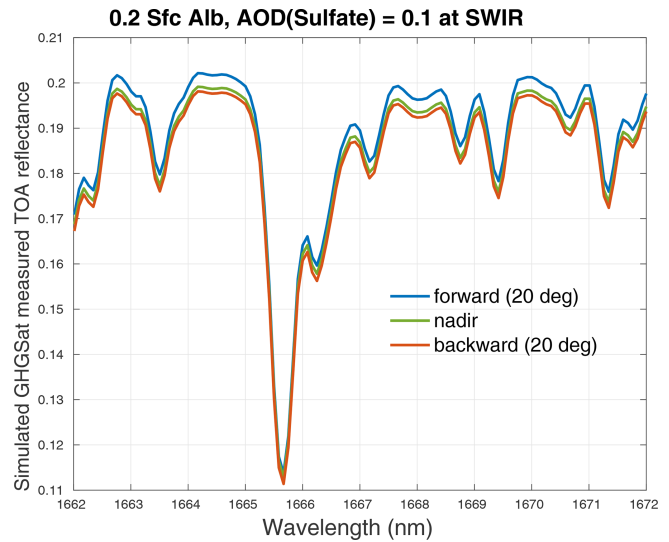


Figure 3. Simulated TOA reflectance measured by the GHGSat instrument at a spectral resolution of 0.3 nm FWHM. The instrument observes the surface with an albedo of 0.2 from different viewing positions as defined in Table 1: forward viewing, nadir, and backward viewing. Sulfate aerosols with an AOD of 0.1 at the SWIR are added near the surface.

spatially resolved ΔX_{CH_4} -only retrieval.

$$\begin{aligned} F^{\text{LFM}}(X) &= \left(X_{\text{alb}} + b_1 n + b_2 n^2 \right) \left[F(\hat{X}) + \left(X_{\text{CH}_4} - \widehat{X}_{\text{CH}_4} \right) \widehat{K}_{X_{\text{CH}_4}} \right] \\ &= \left(X_{\text{alb}} + b_1 n + b_2 n^2 \right) \left[F(\hat{X}) + \Delta X_{\text{CH}_4} \widehat{K}_{X_{\text{CH}_4}} \right] \end{aligned} \tag{5}$$

\hat{X} is the linearization point, at which the state vector in the observation scene is assumed to be in the background state. $\widehat{K}_{\hat{X}}$, the Jacobian that corresponds to different state-vector elements, is a matrix of partial derivatives that describes how the simulated TOA reflectance changes with respect to the elements of the state vector.

$$\mathbf{K} = \frac{\partial F(X)}{\partial X} \tag{6}$$

To account for the bidirectional distribution of surface albedo and the per-pixel signal changes resulting from satellite motion, the forward model includes a second-order polynomial that is a function of the image frame index n (Jervis

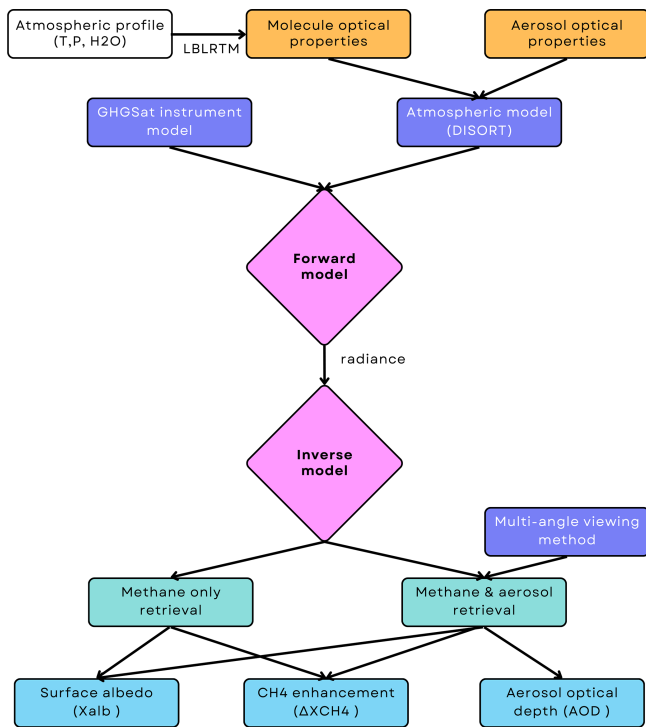


Figure 4. Schematic diagram of the retrieval steps.

et al., 2021). In this study, we employed the LFM model used with current GHGSat instruments and estimated ΔX_{CH_4} and X_{alb} by minimizing the difference between the simulated instrument-measured y and $F^{\text{LFM}}(X)$.

For simultaneous ΔX_{CH_4} and AOD retrieval, we added AOD as an additional variable of interest in the LFM, as depicted below:

$$F^{\text{LFM}} = \left(X_{\text{alb}} + b_1 n + b_2 n^2 \right) \left[F(\hat{X}) + \Delta X_{\text{CH}_4} \widehat{K}_{X_{\text{CH}_4}} + \text{AOD} \widehat{K}_{\text{AOD}} \right]. \quad (7)$$

The applicability of the simultaneous ΔX_{CH_4} and AOD retrieval method mainly comes from two aspects: it enhances the methane gas retrieval accuracy by accounting for the effect of aerosols for GHGSat-like point-source imagers, and it enables the measurement of aerosol plumes using those imagers. By integrating the LBLRTM, DISORT, and the GHGSat instrument model and applying the same inverse model (Eq. 5) utilized in current GHGSat operations, our retrieval results can provide a truthful assessment of the simultaneous ΔX_{CH_4} and AOD retrieval technique on GHGSat-like point-source imagers using the multi-angle viewing method. In the following section, the retrieval method is tested across a wide range of aerosol optical properties, surface albedos, and satellite zenith angle conditions, demonstrating its direct applicability to real measurements.

3 Assessment of two retrieval methods

This paper aims to estimate the impact of aerosols on GHGSat methane retrieval, assess the validity of the multi-angle viewing method for GHGSat aerosol and methane co-retrieval, and understand the algorithm's sensitivity to different input parameters, including surface albedo, SSA, g , and satellite geometry. To achieve this, retrieval experiments were conducted using synthetic data, and the retrieval errors were estimated.

Figure 5 depicts Jacobians with respect to the methane mixing ratio and the AOD with different SSA and g values when the surface albedo is 0.2 and the solar zenith angle is 60° . A negative K_X value indicates that the reflectance at the TOA decreases as the value of the state-vector element X increases. As expected, considering the absorption properties of methane, K_{CH_4} is negative. Similarly, K_{AOD} is also negative in the case of absorbing aerosols (SSA = 0.1). For strongly scattering aerosols (SSA = 0.95) with a high g (0.7) over a dark surface (0.2), K_{AOD} is slightly positive at the forward viewing position and negative at the backward viewing position (Fig. 5b). When the satellite is at the backward viewing position, the aerosol-only scattering is less pronounced because less light scatters towards space in that direction, resulting in a negative K_{AOD} . In contrast, in the forward viewing position, more light is scattered by aerosols towards space, and this effect prevails over the effect of atmospheric-absorption enhancement due to aerosol–surface multiple scattering, resulting in a slightly positive K_{AOD} . This is particularly noticeable when the asymmetry factor, g , is low (0.1). In this case, the dominant factor is the shortening of the light path caused by aerosol-only scattering, which leads to a positive K_{AOD} , regardless of the viewing angle (Fig. 5c). For aerosol with a low g (0.1) over a mid-range albedo (0.5), the competition between aerosol-only scattering and aerosol–surface multiple scattering results in a near-zero K_{AOD} (Fig. 5e).

Figure 5 also compares the Jacobians between the satellite forward (scattering angle 100°) and backward (scattering angle 140°) viewing positions. With high SSA and g values, differences in aerosol Jacobian between the two angles increase, providing more information to the simultaneous retrieval. For simulated GHGSat retrieval using the multi-angle viewing technique, the scattering angle increases from 100 to 140° from forward viewing to backward viewing, as depicted in Fig. 6a. Given a specific asymmetry factor value ($g = 0.78$), the angular distribution of aerosol scattering energy within this scattering angle range is depicted in Fig. 6b. This illustrates that the intensity of scattering energy diminishes as the scattering angle increases, leading a decrease in TOA reflectance. The greater the variation in TOA reflectance at various angles, the richer the aerosol information it can provide for simultaneous retrieval.

As instrument measurements are always subject to noise and errors, it is important to include these in the simulated

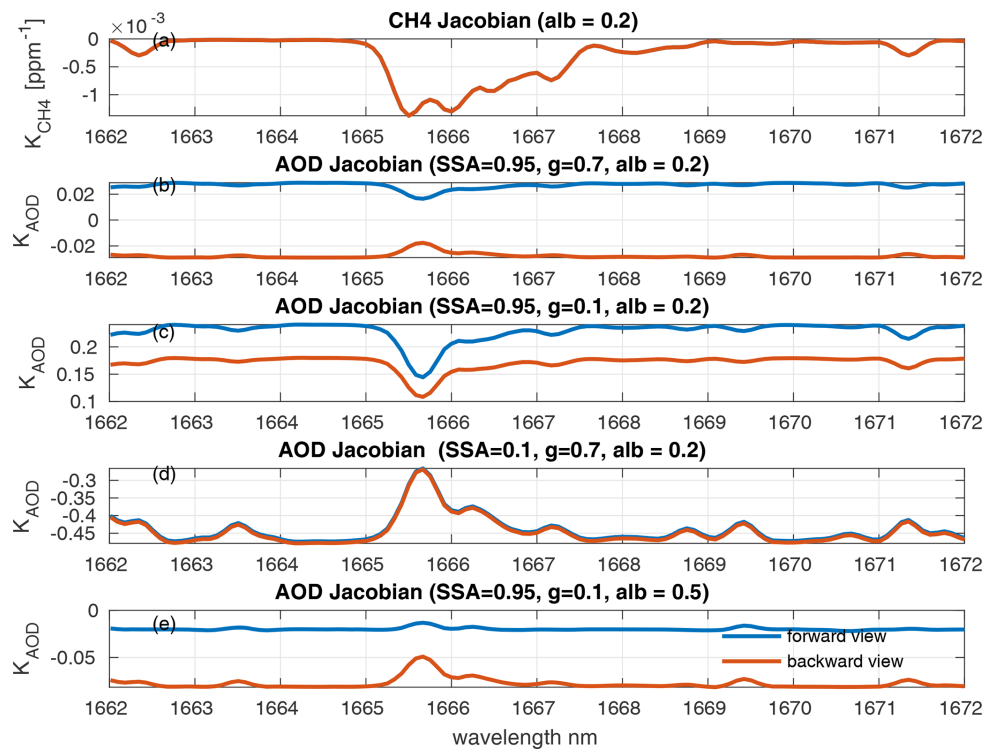


Figure 5. Jacobians of TOA reflectance with respect to (a) the methane mixing ratio; (b) the AOD with an SSA of 0.95, a g of 0.7, and a surface albedo of 0.2; (c) the AOD with an SSA of 0.95, a g of 0.1, and a surface albedo of 0.2; (d) the AOD with an SSA of 0.1, a g of 0.7, and a surface albedo of 0.2; and (e) the AOD with a SSA of 0.95, a g of 0.1, and a surface albedo of 0.5. Aerosols are concentrated near the surface, and the forward and backward viewing-angle settings follow Table 1.

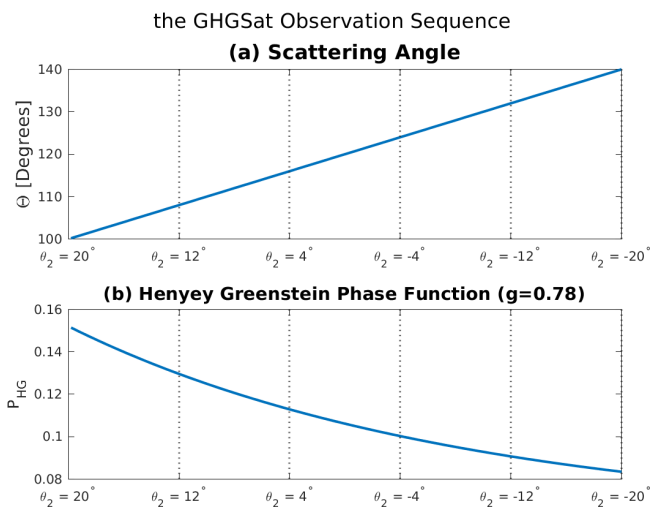


Figure 6. (a) Scattering angle Θ and (b) phase function P_{HG} for $g = 0.78$ as functions of the satellite zenith angle θ_2 during a GHGSat observation sequence when applying the multi-angle viewing method with a maximum satellite zenith angle of 20° .

retrieval process to represent real-world conditions. During the simulated retrieval, white noise and $1/f$ errors with a magnitude of 0.2 % each (calculated as the standard deviation

of the individual noise fields) are added to the TOA reflectance. The background value for the methane mixing ratio is 1.7 ppm. The simulated truths of methane enhancement (ΔX_{CH_4}) and aerosol optical depth (AOD) are 0.1 ppm and 0.1, respectively. We performed 1000 independent retrievals for each aerosol and surface albedo setting, and we quantified the mean bias and standard deviation of the retrieved ΔX_{CH_4} relative to the background to represent the level of accuracy and consistency of the retrieved data.

3.1 The impact of incorporating the AOD and employing the multi-angle viewing method

To assess the extent to which incorporating aerosols and applying the multi-angle viewing method can improve the GHGSat methane retrieval, we conducted retrieval under four conditions: when aerosols are present but not retrieved for the (1) nadir-only methane retrieval and (2) the multi-angle viewing methane retrieval and when aerosols and methane are co-retrieved (3) in the nadir viewing mode and (4) in the multi-angle viewing mode. The mean bias in the retrieved ΔX_{CH_4} and AOD is shown in Fig. 7.

Figure 7a and b indicate that the multi-angle viewing method alone has little impact on the methane retrieval accuracy for the methane-only retrieval. For extreme aerosol

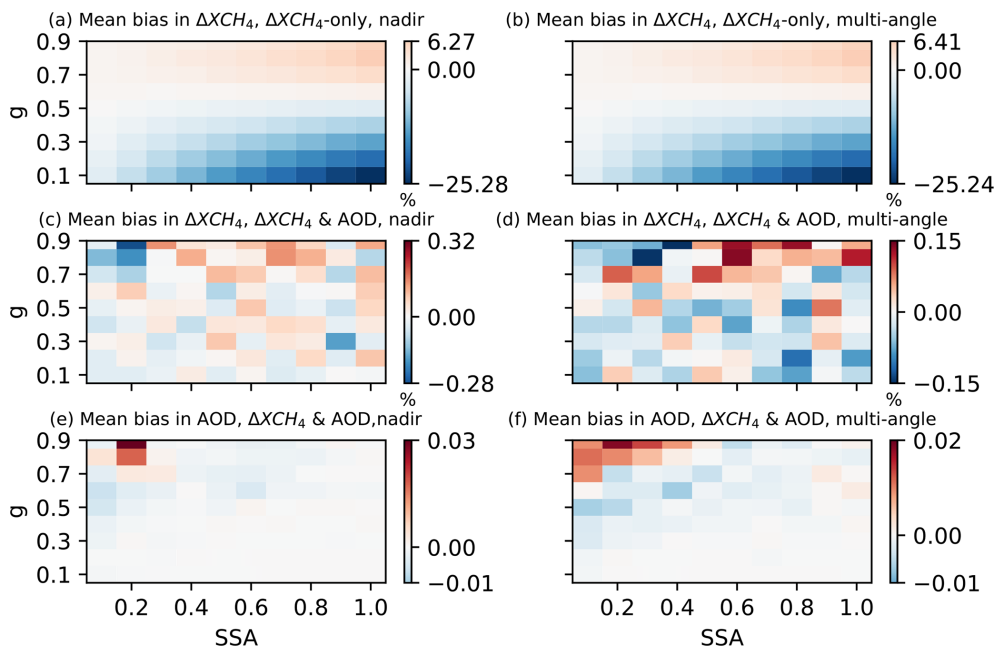


Figure 7. (a, c, e) Nadir-only viewing mode. (b, d, f) Multi-angle viewing mode (Table 1; the scattering angle ranges from 100–140°). (a, b) Mean bias in retrieved ΔX_{CH_4} values when aerosols are present but not retrieved. (c, d) Mean bias in retrieved ΔX_{CH_4} values when aerosols and methane are simultaneously retrieved. (e, f) Mean bias in retrieved AOD values when aerosols and methane are simultaneously retrieved. Retrieval results are displayed as a function of aerosol SSA and g when the surface albedo is 0.2. The simulated truths of ΔX_{CH_4} and AOD are 0.1 ppm and 0.1, respectively. The mean bias in ΔX_{CH_4} is calculated relative to the background methane mixing ratio.

SSA and g values, the mean bias in ΔX_{CH_4} ranges from 6 % to –25 % when aerosols are neglected in the retrieval. After adding AOD as an additional retrieval variable, the mean bias in ΔX_{CH_4} significantly decreased to 0.32 % (Fig. 7c). Further applying the multi-angle viewing method with angles specific in Table 1 reduced the mean bias in ΔX_{CH_4} even further to 0.15 % (Fig. 7d). This suggests that the good performance of aerosol and methane co-retrieval using the multi-angle method largely comes from incorporating AOD as an additional retrieval variable.

As for the AOD retrieval performance, Fig. 7e and f suggest that applying the multi-angle viewing method yields better accuracy in the AOD retrieval than the nadir-only method, with the mean bias in AOD being less than 0.02. In theory, the multi-angle viewing method should provide more information than nadir viewing observations, especially for aerosol retrieval. The relatively modest improvement observed with the multi-angle viewing method in our study compared to the substantial enhancement achieved by adding AOD alone may stem from the instrumental limitation of intensity-only measurements within a single spectral band. Nevertheless, our study continues to employ the multi-angle viewing method for simultaneous aerosol and methane retrieval, as it yields the most significant improvement in retrieval accuracy and precision for both ΔX_{CH_4} and AOD.

3.2 Comparisons between the ΔX_{CH_4} -only retrieval and simultaneous ΔX_{CH_4} and AOD retrieval

To examine the performance of different retrieval methods, we conduct simulated retrieval with a range of surface albedos and aerosol optical properties. We compare two scenarios in terms of the mean bias and standard deviations of retrieved variables (ΔX_{CH_4} , AOD, and X_{alb}): (1) when aerosols are present but not retrieved in the nadir-viewing mode and (2) when both ΔX_{CH_4} and AOD are retrieved simultaneously using the multi-angle viewing method.

3.2.1 Impact of aerosol SSA and g

As we only retrieve the AOD for aerosol-related parameters, unaccounted-for variables such as the aerosol single-scattering albedo (SSA) and asymmetry factor (g) can influence our results. To assess this impact, we fix the background surface albedo at 0.2 and examine how the mean bias and SD vary with different combinations of aerosol SSA and g .

Figure 8a and d display the mean bias of the retrieved ΔX_{CH_4} and X_{alb} values for the ΔX_{CH_4} -only retrieval scenario. The angle setting follows Table 1. When retrieving ΔX_{CH_4} without accounting for aerosols, the ΔX_{CH_4} -only method underestimates ΔX_{CH_4} for situations with low aerosol g and overestimates it in cases with high aerosol g . This occurs because aerosols scatter more light back into space when g is low, reducing the absorption of CH_4 . Con-

versely, when aerosol g is high, increased aerosol–surface multiple scatterings lead to greater atmospheric CH_4 absorption. Figure 8a also shows that the magnitude of the retrieval bias increases with increasing SSA. For a surface albedo of 0.2, the maximum bias in ΔX_{CH_4} for ΔX_{CH_4} -only retrieval can reach -25% relative to the background with extremely high SSA and low g values. These results are in agreement with other studies (Huang et al., 2020). Both increasing SSA and decreasing g enhance the radiation scatter back into space, thereby decreasing the atmospheric-methane absorption. For typical optical-property ranges of aerosols ($\text{SSA} \in [0.86, 0.98]$ and $g \in [0.54, 0.76]$), the mean bias in ΔX_{CH_4} falls between -3.0% and 6.3% for ΔX_{CH_4} -only nadir retrieval. Neglecting aerosols also affects the retrieval of X_{alb} . As shown in Fig. 8d, X_{alb} is underestimated (overestimated) when SSA is small (large).

In contrast, Fig. 9 suggests that simultaneous retrieval of ΔX_{CH_4} and AOD can significantly improve the accuracy of ΔX_{CH_4} retrieval while also retrieving relatively accurate values for AOD and X_{alb} . Using simultaneous retrieval can reduce the mean bias in ΔX_{CH_4} to within 0.1% (Table 2) for typical optical-property ranges of aerosols. As for the consistency of the simultaneous retrieval, Figure 9d indicates that the maximum SD in ΔX_{CH_4} is near to 2.5% , which is slightly higher than that in the ΔX_{CH_4} -only retrieval ($\sim 1.6\%$). This results from the near-zero AOD Jacobian values (Fig. 5b). Although aerosols have little effect on the TOA reflectance under these conditions, their inclusion in the simultaneous retrieval inevitably increases the uncertainty in retrieved ΔX_{CH_4} . As for the AOD results, the mean bias falls within 1.7% for typical aerosol optical-property ranges (Fig. 9b), with the SD showing a slightly high value, suggesting that retrieval uncertainties are larger when aerosol SSA and g vary. In general, the multi-angle method performs better for AOD retrieval when aerosols have a high SSA and a high g , which can be explained by the more pronounced AOD Jacobian differences between forward and backward viewing angles, as indicated by Fig. 5b. In the retrieved surface albedo results (Fig. 9c), the mean bias in ΔX_{alb} is less than 2.1% for typical aerosol optical-property ranges. The mean bias and SD distribution pattern of X_{alb} are similar to those of AOD as a result of the interference of aerosol scattering energy with surface albedo retrieval.

3.2.2 Surface albedo impact

Since the interaction between aerosols and the underlying surface can largely determine the retrieval performance, we further explored the accuracy and precision of the retrieved ΔX_{CH_4} , AOD, and X_{alb} for ΔX_{CH_4} -only retrieval and simultaneous retrieval under different surface albedo conditions.

Figure 8b and e display the distribution of mean bias in ΔX_{CH_4} and that in X_{alb} for ΔX_{CH_4} -only nadir retrieval when aerosol g is fixed at 0.7. As shown in Fig. 8b, neglecting aerosols results in an overestimation (underestimation) of the

retrieved ΔX_{CH_4} with high (low) surface albedo. These results are in agreement with other studies (Butz et al., 2009; Huang et al., 2020), despite the differences in retrieval variables, experiment settings, and instruments. A high surface albedo enhances the surface and aerosol multiple scattering, leading to increased methane absorptions. Conversely, a low surface albedo favours aerosol-only scattering, reducing methane absorptions. As a result, in the case of ΔX_{CH_4} -only retrieval, the bias is most pronounced ($\sim 27\%$) when both aerosol SSA and surface albedo are extremely high. Therefore, it is advisable to refrain from performing methane retrieval over highly reflective surfaces. For commonly encountered aerosol SSA (0.86–0.98) and surface albedo (0.1–0.5) values, the mean bias in ΔX_{CH_4} for ΔX_{CH_4} -only retrieval ranges from -5.9% to 13.1% when g is fixed at 0.7. Similar to Fig. 8d, Fig. 8e suggests that the retrieved X_{alb} value increases with an increase in SSA.

When simultaneously retrieving methane and aerosols, Fig. 10a suggests that the mean bias in ΔX_{CH_4} is significantly reduced to 0.1% when compared with the ΔX_{CH_4} -only retrieval. The SD of the retrieved methane is slightly higher when high-SSA aerosols are present over low-albedo surfaces. This is explained by the near-zero AOD Jacobian values (Fig. 5b), as previously discussed. Moreover, the SDs of the retrieved ΔX_{CH_4} and AOD are a bit higher when SSA is extremely low (0.1). This decrease in retrieval precision results from the positive values in the AOD Jacobian as well as minimal differences in the AOD Jacobian between forward and backward viewing (Fig. 5d), considering the strongly absorbing characteristics of aerosols. In this scenario, it is challenging to distinguish between aerosols and the surface, thereby affecting the CH_4 and aerosol retrieval. The mean bias in the retrieved AOD and X_{alb} is within 1.7% and 0.07% , respectively, for typical values of aerosol SSA and surface albedo ranges ($\text{sfc alb} \in [0.1, 0.5]$ and $\text{SSA} \in [0.86, 0.98]$). In general, the multi-angle viewing technique demonstrates higher accuracy compared with the ΔX_{CH_4} -only retrieval, regardless of surface albedo values, especially when aerosols with stronger scattering abilities are present.

Apart from SSA, it is also interesting to examine how the retrieval bias varies under different combinations of aerosol asymmetry factor and surface albedo. Figure 8c and f present the mean bias in ΔX_{CH_4} and X_{alb} for ΔX_{CH_4} -only retrieval and simultaneous retrieval when aerosol SSA is fixed at 0.95. For ΔX_{CH_4} -only retrieval, ΔX_{CH_4} is underestimated (overestimated) with low (high) surface albedo, especially when g is small. These errors arise because aerosols with low g over dark surfaces tend to scatter more light towards space. However, when the surface is bright, it reflects a larger proportion of the light towards aerosols, and aerosols with low g tend to scatter this light back to the surface again, thereby enhancing methane absorption. The maximum bias in ΔX_{CH_4} for ΔX_{CH_4} -only retrieval is around -50% when both aerosol g and surface albedo are extremely low. For typical values of g

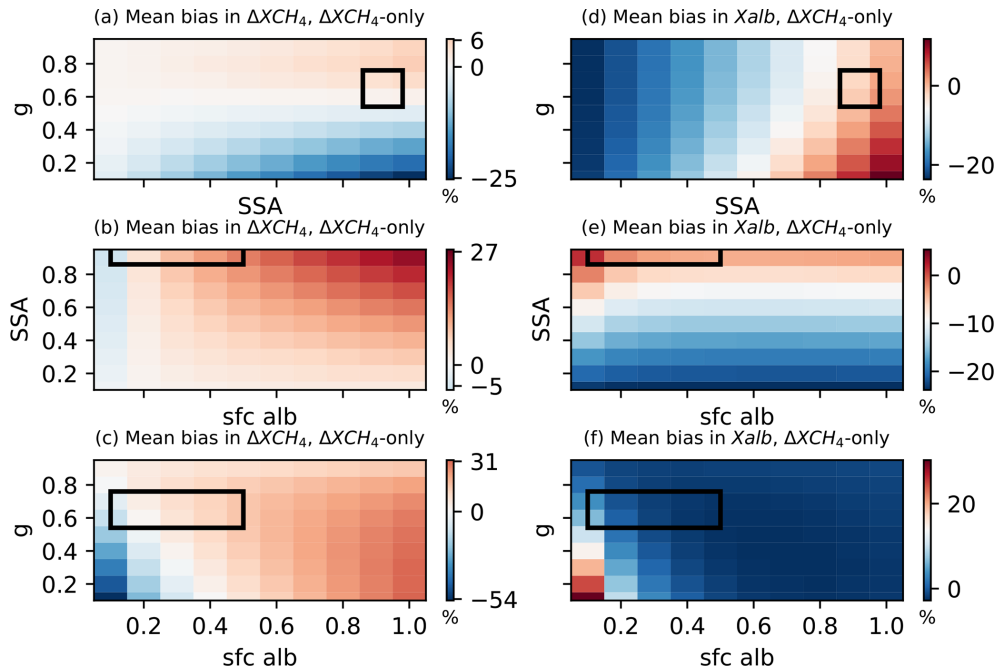


Figure 8. Mean bias of retrieved ΔX_{CH_4} (a, b, c) and X_{alb} (d, e, f) values when aerosols are present but not retrieved in the nadir viewing mode. (a, d) Mean bias as a function of aerosol SSA and g when the surface albedo is 0.2. (b, e) Mean bias as a function of surface albedo and aerosol SSA when aerosol g is 0.7. (c, f) Mean bias as a function of surface albedo and aerosol g when aerosol SSA is 0.95. The black box represents typical values for aerosol optical-property and surface albedo (sfc alb) ranges (SSA \in [0.86, 0.98], $g \in$ [0.54, 0.76] and sfc alb \in [0.1, 0.5]) in the observations. The simulated truths of ΔX_{CH_4} and AOD are 0.1 ppm and 0.1, respectively. The scattering angle ranges from 100–140°.

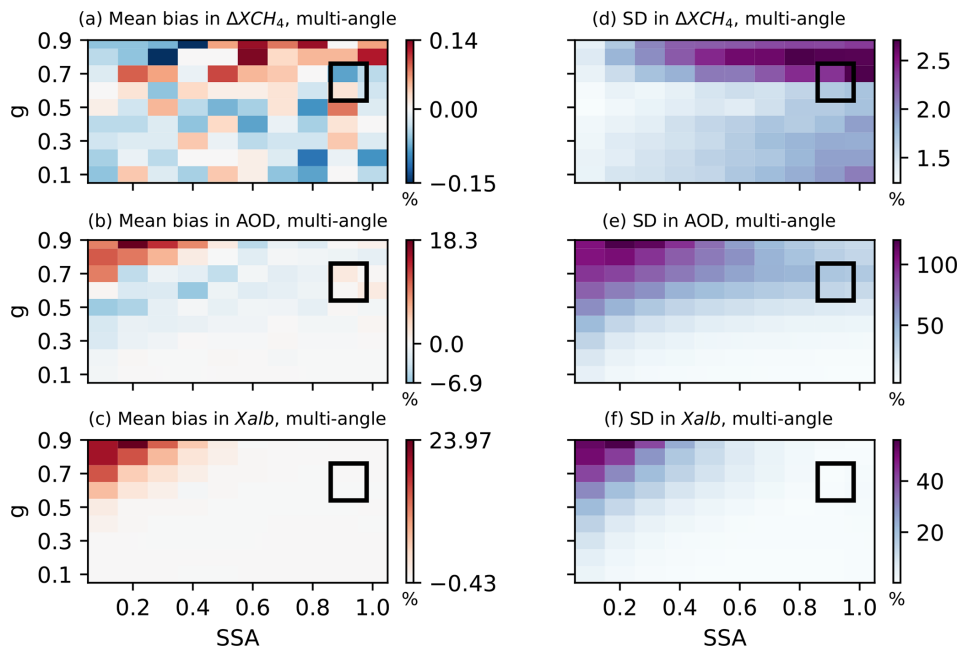


Figure 9. Mean bias (a, b, c) and standard deviations (SDs) (d, e, f) of the retrieved ΔX_{CH_4} , AOD, and X_{alb} as a function of aerosol SSA and g . The simulated truths of ΔX_{CH_4} , AOD, and X_{alb} are 0.1 ppm, 0.1, and 0.2, respectively. The scattering angle ranges from 100–140°. The black box represents the typical values for aerosol optical-property ranges (SSA \in [0.86, 0.98] and $g \in$ [0.54, 0.76]) in the observations.

Table 2. Mean bias and SDs in retrieved ΔX_{CH_4} , AOD, and X_{alb} values for the ΔX_{CH_4} -only retrieval in the nadir viewing mode and for the simultaneous ΔX_{CH_4} and AOD retrieval in the multi-angle viewing mode with a 20° maximum satellite zenith angle. The simulated truths of ΔX_{CH_4} and AOD are 0.1 ppm and 0.1, respectively. The mean bias and SD are given relative to the background values. Experiment nos. 1 to 3 correspond to Sect. 3.2, and experiment no. 4 corresponds to Sect. 4.1. “Correlation coef”: correlation coefficient.

	Mean bias in ΔX_{CH_4}	SD in ΔX_{CH_4}	Mean bias in AOD	SD in AOD	Mean bias in X_{alb}	SD in X_{alb}	Correlation coef (ΔX_{CH_4} and AOD)
Experiment no. 1: SSA \in [0.86, 0.98], $g \in$ [0.54, 0.76], sfc alb = 0.2							
ΔX_{CH_4} -only nadir retrieval	-3.0 % to 6.3 %	1.6 %	-	-	-5.7 % to 3.4 %	0.2 %	-
ΔX_{CH_4} and AOD multi-angle retrieval	-0.1 % to 0.1 %	1.6 % to 2.7 %	-1.7 % to 1.7 %	18.2 % to 48.6 %	-0.07 % to 0.04 %	0.3 % to 2.1 %	-85 % to 30 %
Experiment no. 2: sfc alb \in [0.1, 0.5], SSA \in [0.86, 0.98], $g = 0.7$							
ΔX_{CH_4} -only nadir retrieval	-5.9 % to 13.1 %	1.5 % to 1.6 %	-	-	-6.7 % to 5.4 %	0.2 %	-
ΔX_{CH_4} and AOD multi-angle retrieval	-0.1 % to 0.1 %	1.7 % to 2.6 %	-3.1 % to 1.1 %	8.0 % to 47.0 %	-0.1 % to 0.04 %	0.2 % to 1.83 %	-81 % to 43 %
Experiment no. 3: sfc alb \in [0.1, 0.5], $g \in$ [0.54, 0.76], SSA = 0.95							
ΔX_{CH_4} -only nadir retrieval	-20.5 % to 12.2 %	1.5 % to 1.6 %	-	-	-2.3 % to 10.1 %	0.2 %	-
ΔX_{CH_4} and AOD multi-angle retrieval	-0.1 % to 0.3 %	1.6 % to 2.8 %	-3.0 % to 0.7 %	4.7 % to 39.9 %	0 % to 0.1 %	0.2 % to 1.2 %	-83 % to 52 %
Experiment no. 4: sfc alb \in [0.1, 0.5], max(sat zenith) \in [0° , 20°], SSA = 0.95, $g = 0.7$							
ΔX_{CH_4} -only multi-angle retrieval	-5.7 % to 12.4 %	1.6 % to 1.7 %	-	-	-2.3 % to 5.1 %	0.2 %	-
ΔX_{CH_4} and AOD multi-angle retrieval	-0.1 % to 0.1 %	1.8 % to 2.2 %	-0.2 % to 0.8 %	6.6 % to 26.8 %	0 %	0.2 % to 0.6 %	-65 % to 42 %

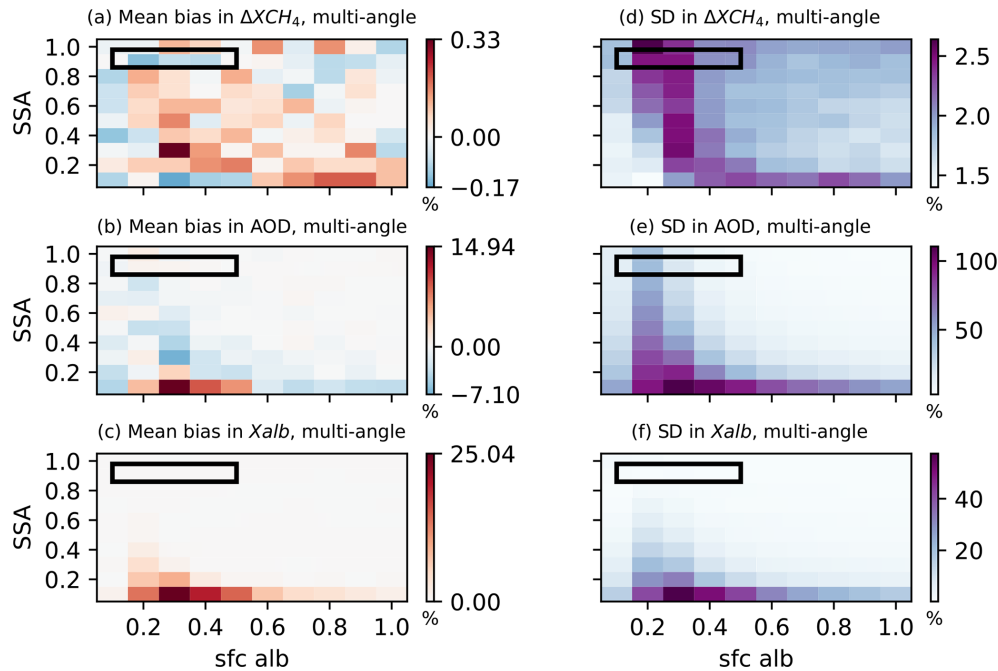


Figure 10. Mean bias (a, b, c) and standard deviations (SDs) (d, e, f) of the retrieved ΔX_{CH_4} , AOD, and X_{alb} as a function of surface albedo and aerosol SSA when aerosol g is 0.7. The simulated truths of ΔX_{CH_4} and AOD are 0.1 ppm and 0.1, respectively. The scattering angle ranges from 100–140°. The black box represents the typical values for aerosol optical-property and surface albedo ranges ($\text{sfc alb} \in [0.1, 0.5]$ and $\text{SSA} \in [0.86, 0.98]$) in the observations.

(0.54–0.76) and surface albedo (0.1–0.5), neglecting aerosols results in a mean bias in ΔX_{CH_4} ranging from -20.5% to 12.2% .

By employing simultaneous retrieval, the mean bias in ΔX_{CH_4} can be reduced to 0.27% (Fig. 11a), demonstrating an enhancement in ΔX_{CH_4} accuracy. An increase in surface albedo enhances surface–aerosol multiple scattering, while a decrease in g enhances aerosol backscattering. This competition effect results in a slope in the distribution of large SD values. Regarding the retrieved AOD and X_{alb} , their mean bias falls within -4.9% and 0.06% (Fig. 11b and c), respectively, in the presence of strongly scattering aerosols ($\text{SSA} = 0.95$).

Overall, in simultaneous ΔX_{CH_4} and AOD retrieval using the multi-angle viewing method, the retrieved ΔX_{CH_4} , AOD, and X_{alb} values generally match very well with the simulated truths across various aerosol optical properties and surface albedo conditions. Table 2 summarizes the mean bias and SDs in the retrieved ΔX_{CH_4} , AOD, and X_{alb} for the ΔX_{CH_4} -only retrieval in the nadir viewing mode and for the simultaneous ΔX_{CH_4} and AOD retrieval in the multi-angle viewing mode, considering typical values of aerosol optical properties and surface albedo encountered in the observations. Using the simultaneous retrieval method, the mean bias and SD in ΔX_{CH_4} fall within the ranges of 0.3% and 2.8% , respectively. Similarly, the mean bias in AOD and X_{alb} remains within 3.1% and 0.1% , respectively. It should be noted that

under certain conditions characterized by near-zero AOD Jacobian values, such as scenarios with high SSA and high g values over a low-albedo surface and high SSA and low g values over a moderately reflective surface, or for positive AOD Jacobian values when SSA is extremely low over surfaces with medium-to-high albedo, we observe a slightly higher SD in simultaneous retrieval. Although the retrieved AOD shows relatively high accuracy, its SD can exceed 10% , suggesting an uncertainty in AOD retrieval when SSA and g are not constrained.

4 Simultaneous retrieval analysis

4.1 The effect of satellite zenith angle on simultaneous retrieval

The discussions above have proved that using the multi-angle viewing method for simultaneous ΔX_{CH_4} and AOD retrieval can significantly improve the retrieval accuracy of ΔX_{CH_4} when compared with the ΔX_{CH_4} -only nadir retrieval. It is still worth investigating whether the retrieval results are highly dependent on the chosen satellite zenith angles. In this section, satellite zenith angles ranging from 0 to 80° are tested in both the ΔX_{CH_4} -only retrieval and the simultaneous retrieval. As shown in Table 3, the scattering angle range broadens with increasing satellite zenith angle magnitude, which could benefit aerosol retrieval, as it leads to

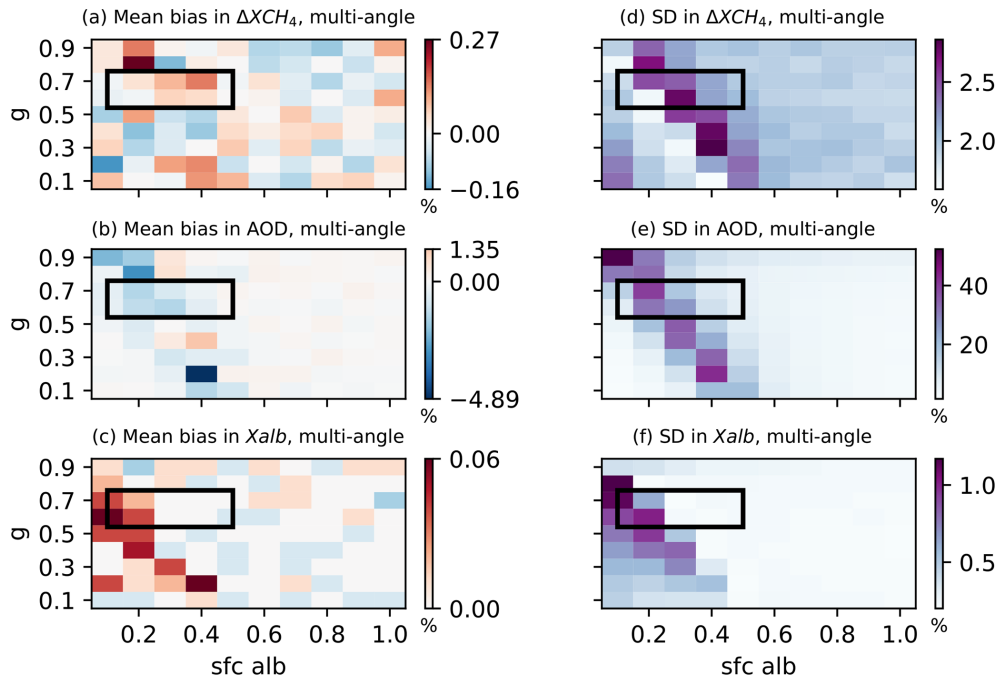


Figure 11. Mean bias (a, b, c) and standard deviations (SDs) (d, e, f) of the retrieved ΔX_{CH_4} , AOD, and X_{alb} as a function of surface albedo and aerosol g when aerosol SSA is 0.95. The simulated truths of ΔX_{CH_4} and AOD are 0.1 ppm and 0.1, respectively. The scattering angle ranges from 100–140°. The black box represents the typical values for aerosol optical-property and surface albedo ranges ($\text{sfc alb} \in [0.1, 0.5]$ and $g \in [0.54, 0.76]$) in the observations.

more distinct differences in TOA reflectance across various satellite viewing positions. However, larger satellite zenith angles could also introduce more bias into methane retrieval because of the slanted-path effect.

Considering aerosols with an AOD of 0.1, a SSA of 0.95, and a g of 0.7, the mean bias and SDs for the ΔX_{CH_4} -only retrieval and for the simultaneous retrieval as a function of surface albedo and the maximum magnitude of the satellite zenith angle are shown in Fig. 12. If aerosols are neglected, the retrieved ΔX_{CH_4} is always overestimated except under the extremely low surface albedo (0.1) condition. The retrieval bias magnitude escalates with growing maximum magnitude of the satellite zenith angle. A larger satellite zenith angle brings a longer light path, which enhances atmospheric absorption and introduces larger retrieval errors. The maximum mean bias in ΔX_{CH_4} for ΔX_{CH_4} -only retrieval can exceed 80 % when the satellite zenith angle exceeds 70°. For typical ranges of the GHGSat satellite zenith angle (10–20°) and the surface albedo (0.1–0.5), the mean bias in ΔX_{CH_4} for ΔX_{CH_4} -only retrieval is –5.7 % to 12.4 %.

For simultaneous ΔX_{CH_4} and AOD retrieval, the mean bias in ΔX_{CH_4} remains below 0.1 %, and it varies little with the chosen satellite zenith angle. This suggests that the multi-angle viewing method is effective for GHGSat-like satellites, regardless of their observation swath. The better retrieval performance of simultaneous retrieval in the multi-angle viewing mode largely results from adding AOD as an additional

predictor instead of applying the multi-angle method, considering that the GHGSat satellite is an intensity-only instrument targeting one specific band.

The magnitude of the SD in ΔX_{CH_4} from the simultaneous retrieval experiences a slight increase and then decreases as the satellite zenith angle magnitude increases. This happens because, with the increase in the satellite's zenith angle, more energy scatters back into space, while a longer light path leads to greater atmospheric absorption. At a specific point, the aerosol Jacobian approaches zero, which introduces relatively high uncertainty into the simultaneous retrieval process.

4.2 Relationship between the retrieved ΔX_{CH_4} and AOD from simultaneous retrieval

Figure 13 illustrates the correlation coefficients between the retrieved ΔX_{CH_4} and AOD for various combinations of SSA, g , surface albedo, and satellite zenith values. The simultaneous retrieval is conducted under four specific conditions using the multi-angle viewing method: (1) when the surface albedo is 0.2, (2) when the g is 0.7, (3) when the SSA is 0.95, and (4) when the SSA is 0.95 and g is 0.7. For conditions (1) to (3), the angle setting follows Table 1, while for condition (4), the angle settings are based on Table 3.

Figure 13a suggests that ΔX_{CH_4} and AOD are negatively correlated for high g values and negatively correlated for low g values when the surface is dark. A high g results in more

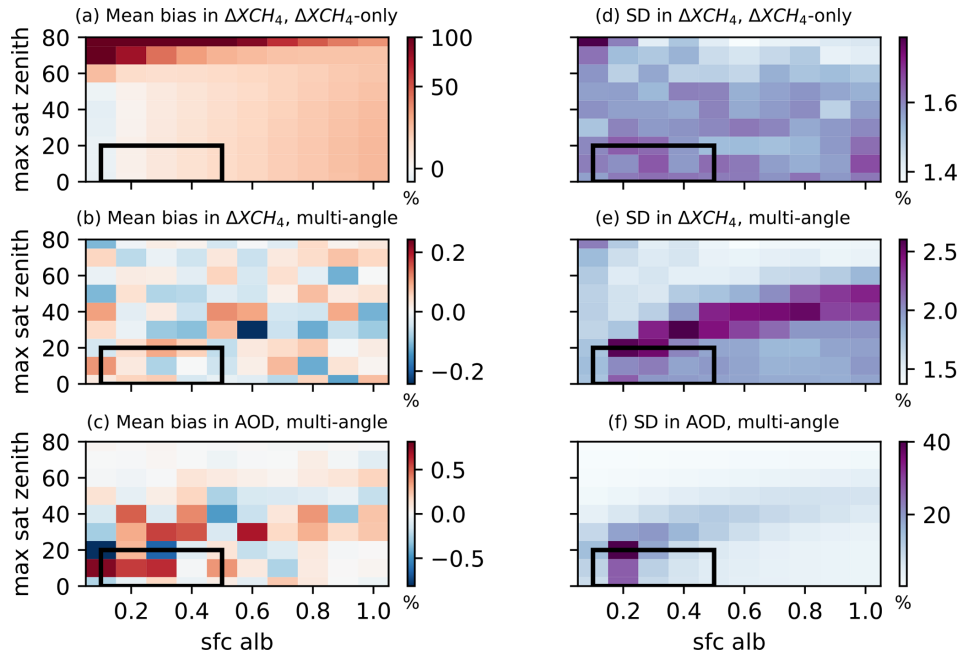


Figure 12. (a) Mean bias and (d) standard deviation (SD) of retrieved ΔX_{CH_4} values when aerosols are present but not retrieved. (b) Mean bias and (e) SD of retrieved ΔX_{CH_4} values for simultaneous ΔX_{CH_4} and AOD retrieval. (c) Mean bias and (f) SD of retrieved AOD values for simultaneous ΔX_{CH_4} and AOD retrieval. The retrieval results are displayed as a function of surface albedo and maximum magnitude of satellite zenith angle when aerosol SSA is 0.95, g is 0.7, and the solar zenith angle is 60° . The satellite is in the multi-angle viewing mode. The black box represents the typical values for the GHGSat satellite zenith angle range and the surface albedo range ($\max(\text{sat zenith}) \theta_2 \in [0^\circ, 20^\circ]$ and $\text{sfc alb} \in [0.1, 0.5]$).

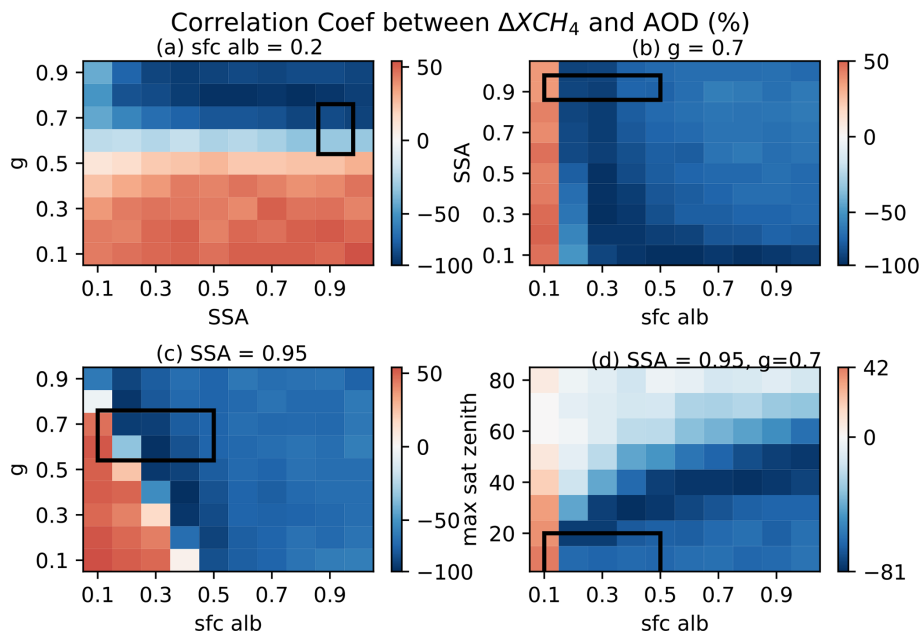


Figure 13. Correlation coefficient (%) between the simultaneously retrieved methane enhancement (ΔX_{CH_4}) and aerosol optical depth (AOD) for varying aerosol types and surface albedo values. (a) Surface albedo is fixed at 0.2. (b) Aerosol g is fixed at 0.7. (c) Aerosol SSA is fixed at 0.95. For panels (a) to (c), the maximum magnitude of the satellite zenith angle is 20° . (d) Aerosol SSA is fixed at 0.95 and g is fixed at 0.7. The black box represents the typical values of the ranges for aerosol optical properties, surface albedo, and solar zenith angle in the GHGSat observations.

Table 3. Satellite zenith angle ranges tested for ΔX_{CH_4} -only retrieval and simultaneous ΔX_{CH_4} and AOD retrieval using the multi-angle viewing method. The solar zenith angle is 60° .

Satellite zenith angle range	0°	-10 to 10°	-20 to 20°	-30 to 30°	-40 to 40°	-50 to 50°	-60 to 60°	-70 to 70°	-80 to 80°
Scattering angle range	120°	110 to 130°	100 to 140°	90 to 150°	80 to 160°	70 to 170°	60 to 180°	50 to 180°	40 to 180°

concentrated forward scattering towards the ground, causing more atmospheric absorption via aerosol–surface multiple scattering. To maintain the relative depth of the CH_4 absorption spectra, less ΔX_{CH_4} needs to be retrieved to balance the effect of the increasing AOD. In Fig. 13b, ΔX_{CH_4} and AOD are positively correlated for low-albedo surfaces and negatively correlated for mid- and high-albedo surfaces when g is 0.7. With a dark surface, increasing the aerosol causes a greater amount of light to be scattered back into space, leaving less light to interact with CH_4 . Consequently, a larger ΔX_{CH_4} is retrieved to counterbalance the impact of the increasing AOD. Figure 13c shows that the correlation between ΔX_{CH_4} and AOD changes from positive to negative with increasing g and surface albedo when SSA is 0.95. This pattern occurs because of the shift in the dominant aerosol-involved physical processes from the aerosol-only scattering effect to the aerosol–surface multiple scattering effect. Figure 13d shows that for aerosols with an SSA of 0.95 and a g of 0.7, ΔX_{CH_4} and AOD are positively (negatively) correlated at low (high) albedo. With increasing satellite zenith angle, the magnitude of the correlation coefficient first increases and then decreases, suggesting that it is still beneficial to apply large scattering angle ranges in the multi-angle viewing method to better distinguish aerosols and methane.

When considering a surface with an albedo of 0.2, a SSA from 0.86 to 0.98, and a g from 0.54 to 0.76, the correlation coefficient between the retrieved ΔX_{CH_4} and AOD falls within the range of -85% to 30% . Similarly, when the SSA is maintained between 0.86 and 0.98, the surface albedo varies from 0.1 to 0.5, and g is fixed at 0.7, the correlation coefficient ranges from -81% to 43% . Lastly, for cases where g ranges from 0.54 to 0.76, the surface albedo spans from 0.1 to 0.5, and SSA is set at 0.95, the correlation coefficient varies from -83% to 52% . In general, the pattern in Fig. 13 is similar to the ΔX_{CH_4} SD pattern in Figs. 9–12, which confirms that the high correlation of ΔX_{CH_4} with AOD results in a larger SD in ΔX_{CH_4} .

4.3 Impact of aerosol and surface albedo uncertainties on simultaneous retrieval

Although aerosol types could be inferred from emission plumes by considering the combustion type and location, the uncertainty that arises from the inaccurate representation of aerosol types and distributions could impact the performance of our simultaneous retrieval. Additionally, assumptions regarding the Lambertian surface and satellite viewing geometry could potentially introduce uncertainties into

surface albedo retrieval. To assess this uncertainty, we employ certain aerosol SSA and g values, height distributions, and surface albedos in the retrieval, while for the simulated GHGSat radiance, we incorporate more complex representations of aerosol type and distributions and surface albedo. The differences between retrieval with fixed (inaccurate) parameters and retrieval with real (accurate) parameters enable us to quantify the uncertainty resulting from the inaccurate representation of these parameters.

4.3.1 Aerosol type uncertainties

Figure 14 presents the differences in the mean bias and standard deviations of retrieved variables between retrieval assuming SSA = 0.95 and $g = 0.7$ for aerosols and retrieval assuming the correct SSA and g (ranging from 0 to 1). These differences could suggest that there is uncertainty in simultaneous retrieval when assuming inaccurate aerosol types. Figure 14a and d show that the uncertainties in the mean bias and SD of ΔX_{CH_4} related to aerosol types range from -5.8% to 2.7% and from -0.2 to 0.9% , respectively, for typical aerosol optical-property values. The uncertainties in the mean bias and SD of AOD fall within -40.2% to 16.1% and within -9.6% to 20% , respectively. Similarly, the uncertainties in the mean bias and SD of X_{alb} range from -5.6% to 5.4% and from -1.5% to 0.39% , respectively. These findings suggest that even with incorrect SSA and g assumptions in the retrieval, the maximum uncertainty induced in the accuracy of the retrieved ΔX_{CH_4} is within 5.8% .

4.3.2 Aerosol height distribution uncertainties

While aerosols primarily reside near the surface at the industrial site, they could also ascend to higher altitudes under favourable atmospheric conditions. Therefore, we examined the uncertainty brought by aerosol height assumptions. We compared the difference between the retrieval when we assume aerosols are near the surface and the retrieval when aerosols are elevated to 5 km. In the latter case, AOD linearly decreases with height, but we still use the near-surface Jacobian calculations in retrieval. Figure 15 shows the uncertainties in simultaneous retrieval when assuming an incomplete aerosol height.

Similar to the uncertainty results related to aerosol types, Fig. 15a and d show that the uncertainty induced by aerosol height in the mean bias and SD of ΔX_{CH_4} ranges from 2.3% to 6.4% and from -0.1% to 0.1% , respectively, for typical values of aerosol optical properties. The mean bias un-

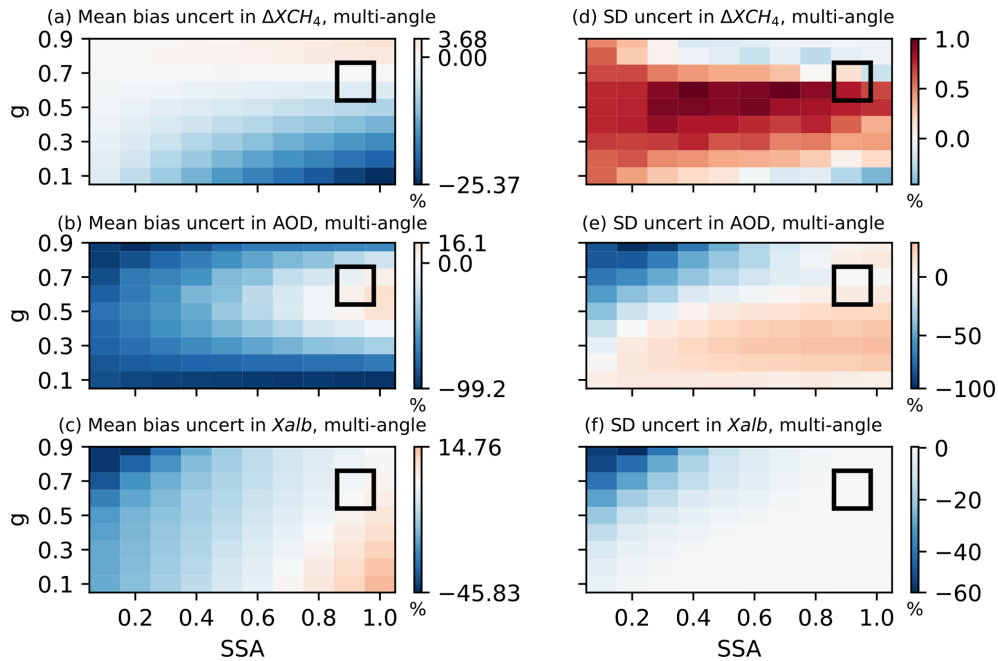


Figure 14. Uncertainties induced by aerosol type in the mean bias (a, b, c) and standard deviations (SD) (d, e, f) of the retrieved ΔX_{CH_4} , AOD, and X_{alb} , assuming aerosols with an SSA of 0.95 and a g of 0.7 in the retrieval. The simulated truths of ΔX_{CH_4} , AOD, and X_{alb} are 0.1 ppm, 0.1, and 0.2, respectively. The scattering angle ranges from 100–140°. The black box represents the typical values for aerosol optical-property ranges (SSA \in [0.86, 0.98] and $g \in$ [0.54, 0.76]) in the observations.

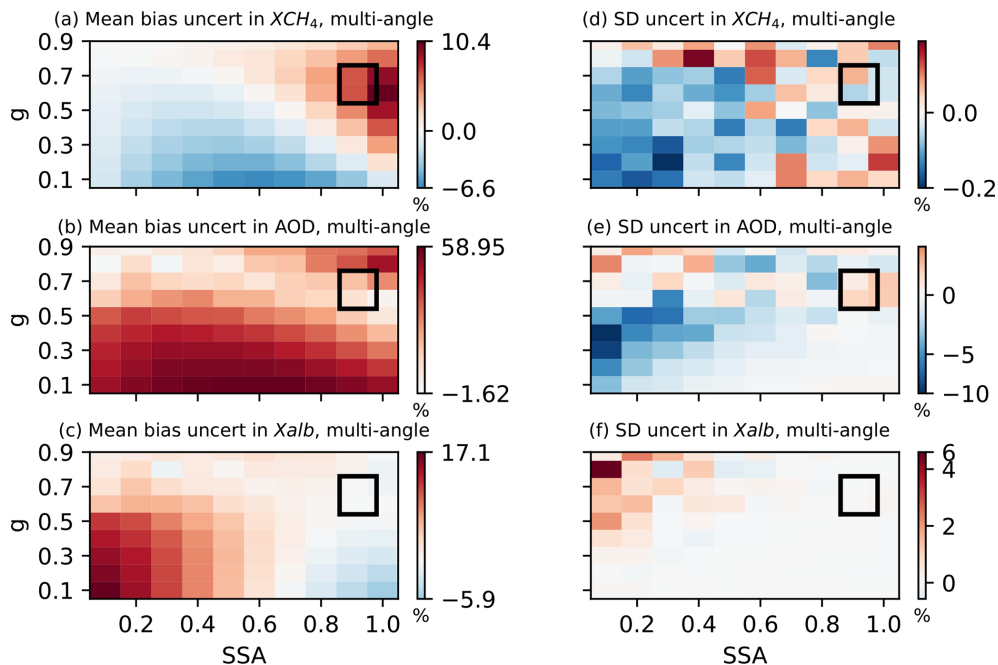


Figure 15. Uncertainties induced by aerosol height distributions in the mean bias (a, b, c) and standard deviations (SDs) (d, e, f) of retrieved ΔX_{CH_4} , AOD, and X_{alb} , assuming near-surface aerosols in the retrieval. The simulated truths of ΔX_{CH_4} , AOD, and X_{alb} are 0.1 ppm, 0.1, and 0.2, respectively. The scattering angle ranges from 100–140°. The black box represents the typical values for aerosol optical-property ranges (SSA \in [0.86, 0.98] and $g \in$ [0.54, 0.76]) in the observations.

certainties for AOD and X_{alb} fall within the ranges of 2.3 % to 41.5 % and -0.8 % to 1.4 %, respectively. The SD uncertainties for ΔX_{CH_4} , AOD, and X_{alb} are generally small, indicating minimal sensitivity of the retrieval precision to the aerosol height distributions.

4.3.3 Surface albedo uncertainties

Although a second-order polynomial was applied in the retrieval to account for the bidirectional distribution of surface albedo, the imperfect representation of surface albedo, particularly in regions with heterogeneous landscapes, could introduce uncertainty into the simultaneous retrieval. To quantify such uncertainty, we compared the differences between the retrieval when we assume the surface albedo is 0.2 and the retrieval with the correct surface albedo values. Figure 16 shows the uncertainties in simultaneous retrieval when assuming imperfect surface albedo.

Figure 16a and d show that the uncertainty in the mean bias and SD of ΔX_{CH_4} resulting from surface albedo variations ranges from -15.1 % to 4 % and from -0.1 % to 0.7 %, respectively, for typical aerosol SSA and surface albedo ranges ($\text{sfc alb} \in [0.1, 0.5]$ and $\text{SSA} \in [0.86, 0.98]$). The mean bias uncertainties for AOD and X_{alb} fall within the ranges of -12.7 % to 37.6 % and -5.9 % to 3.5 %, respectively, while the SD uncertainties for AOD and X_{alb} range from -1.1 % to 31.9 % and from -0.31 % to 2.25 %, respectively.

In summary, the uncertainties in the mean bias and SD of ΔX_{CH_4} induced by inaccurate aerosol types, height distributions, and surface albedo are less than 15.1 % and 0.9 %, respectively. These uncertainties are obtained when assuming near-surface aerosols with fixed SSA (0.95) and g (0.7) and a surface albedo of 0.2 in the retrieval, while simulated radiance, aerosol SSA, g , height distribution, and surface albedo vary across typical observation ranges.

5 Conclusions

This study investigates the impacts of aerosols on GHGSat methane retrieval in the shortwave near-infrared band by exploiting dynamic aerosol scattering behaviour during the GHGSat “multi-angle” observation sequence. Specifically, this research assesses how reliably aerosols can be simultaneously retrieved with methane using the multi-angle viewing method under different aerosol optical-property, surface albedo, and satellite zenith angle conditions. Observing system simulation experiments (OSSEs) are conducted to simulate GHGSat observations and perform retrieval in the presence of white noise and $1/f$ errors. These experiments involve a comparative assessment of retrieval accuracy and precision under two conditions: (1) when aerosols are present but not retrieved in the satellite nadir viewing mode and (2) when both methane mixing-ratio enhancement (ΔX_{CH_4})

and aerosol optical depth (AOD) are retrieved simultaneously in the multi-angle viewing mode.

The general behaviour observed in the ΔX_{CH_4} -only retrieval experiment is that ΔX_{CH_4} is underestimated for low-albedo surfaces and overestimated for high-albedo surfaces when aerosols are not taken into account. The estimated errors in ΔX_{CH_4} for non-aerosol retrieval become more significant as the aerosol single-scattering albedo (SSA) increases and the asymmetry factor (g) decreases. For nadir viewing simulations where AOD is set at 0.1 and the solar zenith angle at 60° , the mean bias in the retrieved ΔX_{CH_4} is most significant when scattering aerosols over bright surfaces are neglected. For a surface with an albedo of 0.2, the bias in ΔX_{CH_4} varies from -3.0 % to 6.3 % for typical aerosol optical properties ($\text{SSA} \in [0.86, 0.98]$ and $g \in [0.54, 0.76]$) (Fig. 9a); for a satellite zenith angle ranging from 0 – 20° and a surface albedo varying between 0.1 and 0.5, the mean bias in ΔX_{CH_4} for ΔX_{CH_4} -only retrieval spans from -5.7 % to 12.4 % (Fig. 12a), assuming an AOD of 0.1, SSA of 0.95, and a g value of 0.7.

Using the multi-angle viewing method for simultaneous ΔX_{CH_4} and AOD retrieval, we find that the bias in retrieved ΔX_{CH_4} is significantly reduced at the modest cost of slightly worse ΔX_{CH_4} precision. Through simultaneous retrieval, the mean bias in ΔX_{CH_4} can be reduced to as low as 0.3 % for the typical ranges of aerosol optical properties, surface albedos, and satellite zenith angles (Table 2). The standard deviation (SD) of ΔX_{CH_4} in simultaneous retrieval experiences a slight increase when aerosols have a minimum impact on the TOA radiance, as indicated by near-zero AOD Jacobian values. Nevertheless, this SD remains within 2.8 %. The uncertainties in the mean bias and SD of ΔX_{CH_4} induced by inaccuracies in aerosol types, height distributions, and the surface albedo are less than 15.1 % and 0.9 %, respectively (Figs. 14–16). The multi-angle viewing method also performs relatively well in AOD retrieval, as characterized by a mean bias of less than 3.1 % (Table 2). The performance assessment shows that retrieving aerosols and methane simultaneously using the multi-angle viewing method is a viable approach for operational application to GHGSat.

The correlation coefficient between simultaneously retrieved AOD and ΔX_{CH_4} switches from positive to negative with increasing surface albedo and decreasing aerosol g (Fig. 13a–c). This transition occurs because the dominant influence of aerosols on the radiance shifts from the aerosol-only scattering effect to the aerosol–surface multiple scattering effect, which suggests that the ability to differentiate between aerosols and methane is highly dependent on the aerosols and surface conditions present.

This study also explored whether the success of the AOD and ΔX_{CH_4} co-retrieval with multi-angle viewing technique is largely determined by the range of scattering angles present in the GHGSat observation sequence. After conducting retrieval over a range of satellite zenith angle values (0 to 80°), results suggest that a broader scattering angle range,

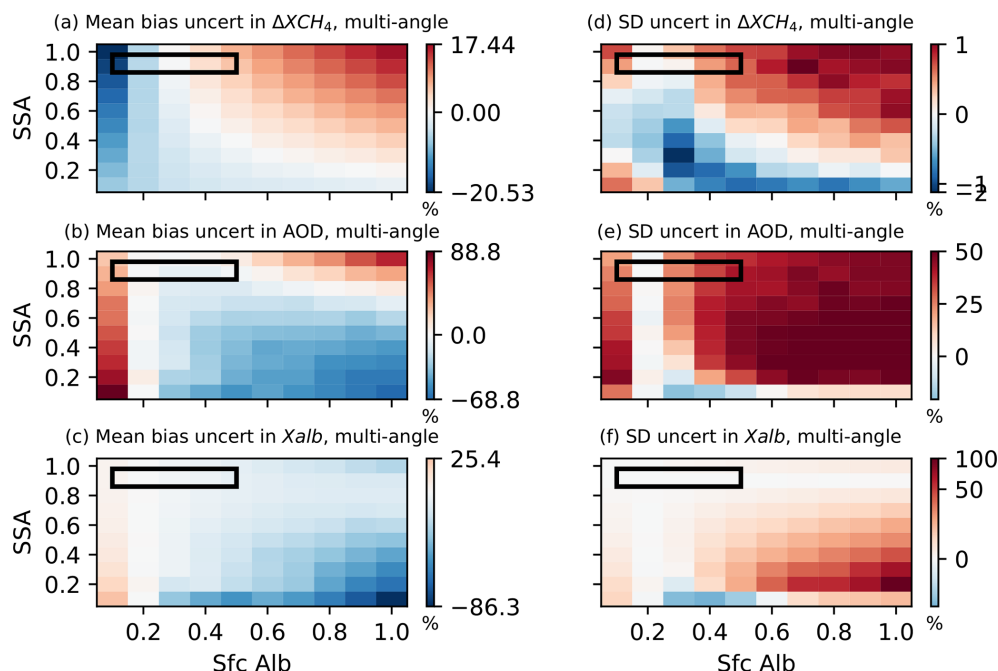


Figure 16. Uncertainties induced by surface albedo in the mean bias (a, b, c) and standard deviations (SD) (d, e, f) of retrieved ΔX_{CH_4} , AOD, and X_{alb} , assuming a surface albedo of 0.2 in the retrieval. The simulated truths of ΔX_{CH_4} and AOD are 0.1 ppm and 0.1, respectively. The scattering angle ranges from 100–140°. The black box represents the typical values for aerosol optical-property and surface albedo ranges (sfc alb \in [0.1, 0.5] and SSA \in [0.86, 0.98]) in the observations.

such as a larger satellite zenith angle, has little impact on the improvement in AOD and ΔX_{CH_4} co-retrieval accuracy and precision. Therefore, the multi-angle viewing method is relatively insensitive to the satellite angle setting for the GHGSat-like instrument when AOD is incorporated into the retrieval.

Finally, future work on the GHGSat retrieval algorithm and a real retrieval test will investigate the feasibility of adding an aerosol retrieval capability to current and future instruments.

Data availability. The atmospheric model and synthetic data used in the assessment can be obtained from Mendeley Data at <https://doi.org/10.17632/jxcmc63p2h.1> (Yu, 2024).

Author contributions. QY, DJ, and YH co-designed the OSSEs. QY and YH developed the radiative transfer model, and DJ provided the GHGSat instrument model. QY led the writing of the manuscript with contributions from DJ and YH.

Competing interests. The contact author has declared that none of the authors has any competing interests.

Disclaimer. Publisher's note: Copernicus Publications remains neutral with regard to jurisdictional claims made in the text, published maps, institutional affiliations, or any other geographical representation in this paper. While Copernicus Publications makes every effort to include appropriate place names, the final responsibility lies with the authors.

Acknowledgements. The authors thank the editor and three anonymous reviewers for comments that lead to improvements in the manuscript.

Financial support. This research has been supported by the Mitacs (grant no. IT16447) and the Canadian Network for Research and Innovation in Machining Technology, Natural Sciences and Engineering Research Council of Canada (grant no. RGPIN-2019-04511).

Review statement. This paper was edited by Jian Xu and reviewed by three anonymous referees.

References

- Aben, I., Hasekamp, O., and Hartmann, W.: Uncertainties in the space-based measurements of CO_2 columns due to scattering in the Earth's atmosphere, *J. Quant. Spectrosc. Ra.*, 104, 450–459, <https://doi.org/10.1016/j.jqsrt.2006.09.013>, 2007.

- Ayash, T., Gong, S. L., Jia, C. Q., Huang, P., Zhao, T. L., and Lavoue, D.: Global modeling of multicomponent aerosol species: Aerosol optical parameters, *J. Geophys. Res.-Atmos.*, 113, D12203, <https://doi.org/10.1029/2007JD008968>, 2008.
- Boiyo, R., Kumar, K. R., Zhao, T., and Guo, J.: A 10-Year Record of Aerosol Optical Properties and Radiative Forcing Over Three Environmentally Distinct AERONET Sites in Kenya, East Africa, *J. Geophys. Res.-Atmos.*, 124, 1596–1617, <https://doi.org/10.1029/2018JD029461>, 2019.
- Butz, A., Hasekamp, O. P., Frankenberg, C., and Aben, I.: Retrievals of atmospheric CO₂ from simulated spaceborne measurements of backscattered near-infrared sunlight: accounting for aerosol effects, *Appl. Optics*, 48, 3322, <https://doi.org/10.1364/AO.48.003322>, 2009.
- Butz, A., Galli, A., Hasekamp, O., Landgraf, J., Tol, P., and Aben, I.: TROPOMI aboard Sentinel-5 Precursor: Prospective performance of CH₄ retrievals for aerosol and cirrus loaded atmospheres, *Remote Sens. Environ.*, 120, 267–276, <https://doi.org/10.1016/j.rse.2011.05.030>, 2012.
- Calvello, M., Caggiano, R., Esposito, F., Lettino, A., Sabia, S., Summa, V., and Pavese, G.: IMAA (Integrated Measurements of Aerosol in Agri valley) campaign: Multi-instrumental observations at the largest European oil/gas pre-treatment plant area, *Atmos. Environ.*, 169, 297–306, <https://doi.org/10.1016/j.atmosenv.2017.09.026>, 2017.
- Chan Miller, C., Roche, S., Wilzewski, J. S., Liu, X., Chance, K., Souri, A. H., Conway, E., Luo, B., Samra, J., Hawthorne, J., Sun, K., Staebell, C., Chulakadabba, A., Sargent, M., Benmergui, J. S., Franklin, J. E., Daube, B. C., Li, Y., Laughner, J. L., Baier, B. C., Gautam, R., Omara, M., and Wofsy, S. C.: Methane retrieval from MethaneAIR using the CO₂ Proxy Approach: A demonstration for the upcoming MethaneSAT mission, *EGU-sphere* [preprint], <https://doi.org/10.5194/egusphere-2023-1962>, 2023.
- Chen, X., Yang, D., Cai, Z., Liu, Y., and Spurr, R.: Aerosol Retrieval Sensitivity and Error Analysis for the Cloud and Aerosol Polarimetric Imager on Board TanSat: The Effect of Multi-Angle Measurement, *Remote Sensing*, 9, 183, <https://doi.org/10.3390/rs9020183>, 2017.
- Clough, S. A., Shephard, M. W., Mlawer, E. J., Delamere, J. S., Iacono, M. J., Cady-Pereira, K., Boukabara, S., and Brown, P. D.: Atmospheric radiative transfer modeling: a summary of the AER codes, *J. Quant. Spectrosc. Ra.*, 91, 233–244, <https://doi.org/10.1016/j.jqsrt.2004.05.058>, 2005.
- Connor, B., Bösch, H., McDuffie, J., Taylor, T., Fu, D., Frankenberg, C., O'Dell, C., Payne, V. H., Gunson, M., Pollock, R., Hobbs, J., Oyafuso, F., and Jiang, Y.: Quantification of uncertainties in OCO-2 measurements of XCO₂: simulations and linear error analysis, *Atmos. Meas. Tech.*, 9, 5227–5238, <https://doi.org/10.5194/amt-9-5227-2016>, 2016.
- Frankenberg, C., Hasekamp, O., O'Dell, C., Sanghavi, S., Butz, A., and Worden, J.: Aerosol information content analysis of multi-angle high spectral resolution measurements and its benefit for high accuracy greenhouse gas retrievals, *Atmos. Meas. Tech.*, 5, 1809–1821, <https://doi.org/10.5194/amt-5-1809-2012>, 2012.
- Houweling, S., Hartmann, W., Aben, I., Schrijver, H., Skidmore, J., Roelofs, G.-J., and Breon, F.-M.: Evidence of systematic errors in SCIAMACHY-observed CO₂ due to aerosols, *Atmos. Chem. Phys.*, 5, 3003–3013, <https://doi.org/10.5194/acp-5-3003-2005>, 2005.
- Huang, J., Arnott, W. P., Barnard, J. C., and Holmes, H. A.: Theoretical Uncertainty Analysis of Satellite Retrieved Aerosol Optical Depth Associated with Surface Albedo and Aerosol Optical Properties, *Remote Sensing*, 13, 344, <https://doi.org/10.3390/rs13030344>, 2021.
- Huang, Y., Natraj, V., Zeng, Z.-C., Kopparla, P., and Yung, Y. L.: Quantifying the impact of aerosol scattering on the retrieval of methane from airborne remote sensing measurements, *Atmos. Meas. Tech.*, 13, 6755–6769, <https://doi.org/10.5194/amt-13-6755-2020>, 2020.
- Jacob, D. J., Varon, D. J., Cusworth, D. H., Dennison, P. E., Frankenberg, C., Gautam, R., Guanter, L., Kelley, J., McKeever, J., Ott, L. E., Poulter, B., Qu, Z., Thorpe, A. K., Worden, J. R., and Duren, R. M.: Quantifying methane emissions from the global scale down to point sources using satellite observations of atmospheric methane, *Atmos. Chem. Phys.*, 22, 9617–9646, <https://doi.org/10.5194/acp-22-9617-2022>, 2022.
- Jervis, D., McKeever, J., Durak, B. O. A., Sloan, J. J., Gains, D., Varon, D. J., Ramier, A., Strupler, M., and Tarrant, E.: The GHGSat-D imaging spectrometer, *Atmos. Meas. Tech.*, 14, 2127–2140, <https://doi.org/10.5194/amt-14-2127-2021>, 2021.
- Lorente, A., Borsdorff, T., Butz, A., Hasekamp, O., van de Brugh, J., Schneider, A., Wu, L., Hase, F., Kivi, R., Wunch, D., Pollard, D. F., Shiomi, K., Deutscher, N. M., Velasco, V. A., Roehl, C. M., Wennberg, P. O., Warneke, T., and Landgraf, J.: Methane retrieved from TROPOMI: improvement of the data product and validation of the first 2 years of measurements, *Atmos. Meas. Tech.*, 14, 665–684, <https://doi.org/10.5194/amt-14-665-2021>, 2021.
- Maasackers, J. D., Varon, D. J., Elfarsdóttir, A., McKeever, J., Jervis, D., Mahapatra, G., Pandey, S., Lorente, A., Borsdorff, T., Foorhuis, L. R., Schuit, B. J., Tol, P., van Kempen, T. A., van Hees, R., and Aben, I.: Using satellites to uncover large methane emissions from landfills, *Science Advances*, 8, eabn9683, <https://doi.org/10.1126/sciadv.abn9683>, 2022.
- Parker, R. J., Webb, A., Boesch, H., Somkuti, P., Barrio Guillo, R., Di Noia, A., Kalaitzi, N., Anand, J. S., Bergamaschi, P., Chevallier, F., Palmer, P. I., Feng, L., Deutscher, N. M., Feist, D. G., Griffith, D. W. T., Hase, F., Kivi, R., Morino, I., Notholt, J., Oh, Y.-S., Ohyama, H., Petri, C., Pollard, D. F., Roehl, C., Sha, M. K., Shiomi, K., Strong, K., Sussmann, R., Té, Y., Velasco, V. A., Warneke, T., Wennberg, P. O., and Wunch, D.: A decade of GOSAT Proxy satellite CH₄ observations, *Earth Syst. Sci. Data*, 12, 3383–3412, <https://doi.org/10.5194/essd-12-3383-2020>, 2020.
- Sanghavi, S., Nelson, R., Frankenberg, C., and Gunson, M.: Aerosols in OCO-2/GOSAT retrievals of XCO₂: An information content and error analysis, *Remote Sens. Environ.*, 251, 112053, <https://doi.org/10.1016/j.rse.2020.112053>, 2020.
- Stamnes, K., Tsay, S.-C., Wiscombe, W., and Jayaweera, K.: Numerically stable algorithm for discrete-ordinate-method radiative transfer in multiple scattering and emitting layered media, *Appl. Optics*, 27, 2502–2509, <https://doi.org/10.1364/AO.27.002502>, 1988.
- Thompson, S. N., van Diedenoven, B., Colarco, P. R., Castellanos, P., Lian, E., and Martins, J. V.: Analysis of Scattering Angle Sampling by Multi-Angle Imaging Polarimeters for Differ-

- ent Orbit Geometries, *Frontiers in Remote Sensing*, 3, 836262, <https://doi.org/10.3389/frsen.2022.836262>, 2022.
- Toublanc, D.: Henyey–Greenstein and Mie phase functions in Monte Carlo radiative transfer computations, *Appl. Optics*, 35, 3270–3274, <https://doi.org/10.1364/AO.35.003270>, 1996.
- Tzanis, C. and Varotsos, C. A.: Tropospheric aerosol forcing of climate: A case study for the greater area of Greece, *Int. J. Remote Sens.*, 29, 2507–2517, <https://doi.org/10.1080/01431160701767575>, 2008.
- Varon, D. J., McKeever, J., Jervis, D., Maasackers, J. D., Pandey, S., Houweling, S., Aben, I., Scarpelli, T., and Jacob, D. J.: Satellite Discovery of Anomalously Large Methane Point Sources From Oil/Gas Production, *Geophys. Res. Lett.*, 46, 13507–13516, <https://doi.org/10.1029/2019GL083798>, 2019.
- Wang, C., Yang, P., Platnick, S., Heidinger, A. K., Baum, B. A., Greenwald, T., Zhang, Z., and Holz, R. E.: Retrieval of Ice Cloud Properties from AIRS and MODIS Observations Based on a Fast High-Spectral-Resolution Radiative Transfer Model, *J. Appl. Meteorol. Clim.*, 52, 710–726, <https://doi.org/10.1175/JAMC-D-12-020.1>, 2013.
- Yu, Q.: Accounting for Aerosols Effect in GHGSat Methane Retrieval, Version 1, Mendeley Data [data set], <https://doi.org/10.17632/jxcmc63p2h.1>, 2024.
- Yu, Q. and Huang, Y.: A Dissection of the Inter-Model Spread of the Aerosol Direct Radiative Effect in CMIP6 Models, *Geophys. Res. Lett.*, 50, e2023GL105112, <https://doi.org/10.1029/2023GL105112>, 2023a.
- Yu, Q. and Huang, Y.: Distributions and Trends of the Aerosol Direct Radiative Effect in the 21st Century: Aerosol and Environmental Contributions, *J. Geophys. Res.-Atmos.*, 128, e2022JD037716, <https://doi.org/10.1029/2022JD037716>, 2023b.